Journal of the Korean Physical Society, Vol. 77, No. 2, July 2020, pp. 177∼185

Non-Positive Corrections and Variance Models for Iterative Post-Log Reconstruction of Extremely Low-Dose CT Data

Soo Mee Kim*
ICT R&D Unit, Korea Institute of Ocean Science & Technology, Busan 49111, Korea

Tzu-Cheng Lee and Paul E Kinahan
Department of Radiology, University of Washington, Seattle, WA 98195, USA

(Received 10 March 2020; revised 27 May 2020; accepted 28 May 2020)

In extremely low-dose protocols to reduce radiation dose to patients, computed tomography (CT) images suffer from increased bias and low signal-to-noise ratio in measurements. In this study, we consider three different non-positive corrections, flip, truncation and mean-preserving filter (MPF), affecting the measurement mean, propose a new variance expression for weights in weighted least-squares (WLS) reconstruction, and evaluate the impact on changes in the mean and variance of measurements. We simulated 1000 polychromatic CT sinograms of a chest phantom, including realistic levels of quantum and electronic noises. For the simulated scenario of 80 kVp and 0.5 mAs, compared to the conventional threshold and flip methods, the mean-preserving filter reduced the bias in post-log sinogram values by up to five times. Simple weights in WLS reconstruction that neglected the effect of non-positive correction limited improvements in the image quality. The advanced variance estimates considering electronic noise and the effect of pre-processing on the variance change made both WLS and penalized WLS reconstructions improve. Although the image quality improvement from a WLS reconstruction based on a Gaussian post-log distribution is inherently limited, the proposed method for estimating the post-log variance including electronic noise and the effect of pre-corrections from a single measurement leads to some improvements in variance estimates for post-log CT data and showed the feasibility of post-log iterative reconstruction for extremely low-dose CT imaging.

Keywords: CT iterative reconstruction, Low-dose CT imaging, Statistical post-log CT model
DOI: 10.3938/jkps.77.177

I. INTRODUCTION

Recently, the widespread use of computed tomography (CT) for disease diagnosis and treatment has led to growing concerns on increased radiation dose to patients, especially pediatric patients. Particularly, the repeated CT scans for treatment monitoring, time-lapse imaging of brain perfusion, or cardiac gating may cause an excessive increase in the cumulative patient dose [1–6]. Thus, low dose protocols were proposed by decreasing the X-ray intensity as low as possible while maintaining clinically acceptable image quality [7–12]. In this study, we considered an extremely low-dose acquisition protocol, which is 10 times lower than the current low-dose clinical protocols [13]. Figure 1 shows a respiratory motion artifact, *i.e.*, spill-over of liver to lung, in a static CT image (b) that causes positron emission tomography (PET) (a) attenuation to over-correct. Further CT dose reduction makes respiratory gating PET/CT more robust with successive CT-based attenuation map acquisitions at multiple time phases in one respiratory cycle.

In extremely low-dose protocols, the CT images suffer from increased bias and too much noise in measurements.

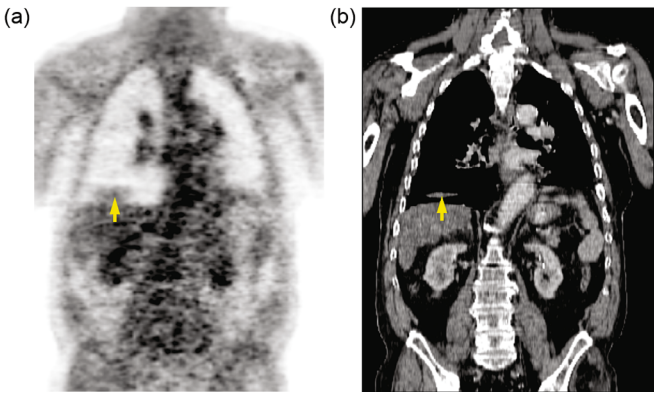

Fig. 1. (a) Respiratory gating PET with a (b) static CT attenuation correction.

*E-mail: smeekim@kiost.ac.kr

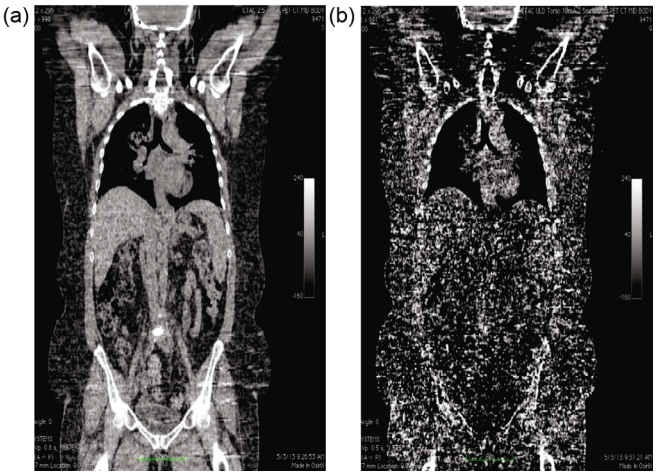

Fig. 2. (a) Standard CT (48 mAs, CTDIvol of 3.3 mGy) and (b) lowest dose CT (5 mAs, CTDIvol of 0.3 mGy).

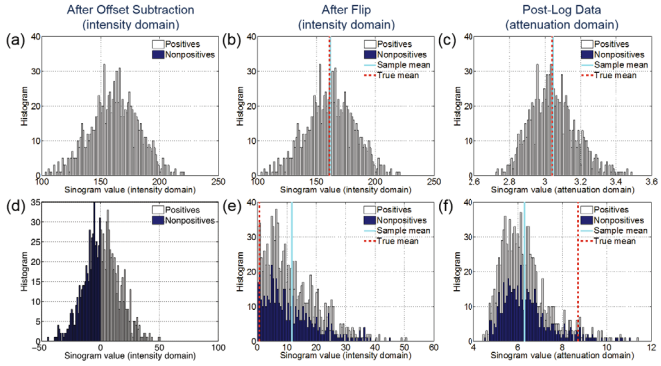

Fig. 3. Histogram of 1000 realizations of two x-rays that undergo a moderate (top) and an extremely high (bottom) attenuation through a chest phantom: (a, d) after offset subtraction in the intensity domain, (b, e) after flip non-positivity correction in the intensity domain, and (c, f) after having taken the logarithm in the attenuation domain.

Figure 2 compares the image from standard low-dose (48 mAs, 120 kVp, CTDIvol of 3.3 mGy) at ALARP (as low as reasonably practicable) to that from the practically lowest (5 mAs, 120 kVp, CTDIvol of 0.3 mGy) dose in a real commercial CT scanner. Numerous efforts to improve the image quality from extremely low-dose acquisitions were present by using denoising techniques in sonogram [14–18] or image domains [19,20] and iterative reconstructions (IRs) [21,22]. Here, we focused on iterative reconstruction, which has potential for improving low-dose imaging with more appropriate noise models for the CT detection process [23–26]. Two groups of models, pre-log and post-log models, can be used to express CT measurements. Currently, although most commercial systems provide post-log IRs, the statistical models appropriate for expressing CT measurements taken under low-dose CT protocols are still the subjects of debate [27,28]. The pre-log measurement model is considered for extremely low-dose CT scans because it has potential for the direct expression of raw measurements and the avoidance of pre-processes related to the logarithm operation for post-log conversion of the raw data. Fu *et al.* investigated pre-log and post-log statistical models for a model-based iterative reconstruction (MBIR) framework for the open question of what is a suitable statistical model for real CT measurements [28]. The simulation and the clinical results show that the pre-log MBIR can accomplish better quantitative accuracy than the post-log MBIR at ultra-low doses and that the pre-log IR had potential for use in new ultra-low-dose CT applications. Fu *et al.* also they mentioned that the post-log IR with sophisticated pre-processing and a less noisy weight could be improved.

Because most current real CT scanners record only post-log sinograms in the energy-integrating mode, we are curious about the effects of post-log IR with robust pre-processing techniques and more appropriate noise statistics under ultra-low-dose CT. One inherent limitation of post-log IR is the way in which the non-positive sinogram values are treated prior to logarithm operation due to the more emphatic electronic noise of the data acquisition system (DAS) in the measured signal. Figure 3 shows that histograms of 1000 realizations of two detector bins that could detect X-rays undergoing the least and the most attenuation through the patient. The upper histograms (a to c) of the least attenuation bin maintained the shapes of the distributions after offset subtraction and a flipping non-positive correction before the logarithm. On the other hand, the bottom histograms (d to f) of the most attenuation bin were distorted because many non-positive realizations of the low mean raw signal were generated and the non-positive values biased the positive area of the histogram distribution. Electronic noise is dominant in extremely low-dose CT data, and pre-corrections, such as the non-positivity correction on the intensity domain, cause large changes in the statistics of the measured data. In this study, we adopted a mean-preserving filter (MPF) to reduce the bias caused by the pre-processes and proposed a new variance model to include the resultant changes from MPF step.

The signal detection and the noise distribution can be expressed by using a cascade of random processes, and several variants of noise models have been proposed to represent the realistic detection statistics of energy-integrating CT signals [29–31]. Here, we investigated the impact of the first- and the second-order statistics, mean and variance of CT data, on iterative reconstruction, and the weighted least-squares (WLS) inverse problem of extremely low-dose post-log CT data, and we proposed an advanced variance expression, including the effect of pre-corrections in the intensity domain, to make the WLS reconstruction robust. We consider three different non-positive corrections affecting the measurement mean and propose a new variance expression for the weights in

WLS reconstruction, and we evaluate the impacts on the changes in the mean and the variance of the measurements.

II. METHODS

We consider a WLS post-log reconstruction, which is defined from a second-order Taylor series expansion of a Poisson log-likelihood, $L(\boldsymbol{\mu})$ [32]:

$$\begin{aligned}\hat{\boldsymbol{\mu}} &= \underset{\mu}{\operatorname{argmin}}\{-L(\boldsymbol{\mu})\} \\ &\approx \underset{\mu}{\operatorname{argmin}} \left\{ \frac{1}{2} \sum_i W_i (p_i - \langle \boldsymbol{D}\mu \rangle_i)^2 \right\} . \end{aligned} \tag{1}$$

In Eq. (1), $\langle \boldsymbol{D}\mu \rangle$ is a projection operator to estimate the mean sinogram from a given attenuation medium distribution ($\boldsymbol{\mu}$), and $\boldsymbol{D}$ is a system matrix for CT imaging. W_i is the weight indicating the reliability of the measurement in the i-th sinogram element, and it is defined with the projection variance. The accuracies of the statistical mean and variance models in CT sinograms affect the data fidelity and the weighting terms in the WLS, respectively. Data fidelity is the mean difference between the measured (p_i) and the estimated projection data ($\langle \boldsymbol{D}\mu \rangle_i$) in the post-log data domain. In the extremely low-dose scenario, the estimated projection data would be biased from the original mean of the real measurement due to conventional pre-processing such as offset subtraction and non-positivity correction. As a minimum variance estimator, the weighting term of the WLS needs to define with the variance of the measurements; however, it is limited to obtaining the projection variance from a single scan.

1. Analysis of Impact on the Statistical Mean Model in CT Sinograms

The post-log projection data (p_i) in the attenuation domain come from the measured pre-log data (λ_i) in the intensity domain by taking logarithms:

$$\boldsymbol{p} = -\log \left(\frac{f(\lambda - \text{Offset})}{I_0 - \text{Offset}} \right) , \tag{2}$$

where I_0 is the influx X-ray intensity. Conventionally, pre-log data go through pre-processing such as offset subtraction and non-positivity correction (f) afore the log conversion. In this study, three non-positivity corrections, flip (FL) and truncation (TH) methods, and a mean-preserving filter (MPF), were investigated in terms of bias from the true mean of the measurement.

The flip method takes the absolute value of a negative value of the offset-subtracted sinogram ($\boldsymbol{X}$) and replaces zero value with the threshold value (ε) as follows:

$$f_{\text{FL}}(X;\varepsilon) = \begin{cases} \varepsilon, & X = 0 \\ |X| & \text{otherwise} \end{cases} . \tag{3}$$

A smaller mean of the projection data typically leads to a larger bias after flip-based correction because flipping the non-positive values tends to shift the mean in the positive direction. The truncation method simply changes a non-positive value to the threshold value (ε):

$$f_{\text{TH}}(X;\varepsilon) = \begin{cases} X, & X > \varepsilon \\ \varepsilon & \text{otherwise} \end{cases} . \tag{4}$$

The threshold is a key parameter to minimize bias from the true projection mean. For the flip and the truncation methods, the ε was computed given a water medium and the maximum path length of X-ray as follows:

$$\varepsilon = I_0 \exp(-\mu_{\text{water}} \cdot L_{\max}) , \tag{5}$$

where μ_{water} is a uniform attenuation coefficient distribution of a water medium at 70 keV within the boundary of an elliptical object. The maximum path length, $L_{\max}$, was set to the intersecting length of the central X-ray path with the elliptical water medium.

The MPF [33] has two successive processing steps of converting non-positives to new values through Eq. (6) and then spreading forward the error ($\boldsymbol{E}$) between the old and the new values into neighbor sinogram bins:

$$f_{\text{MPF}}(X;\alpha) = \alpha \log \left(\exp \left(\frac{X}{\alpha} \right) + 1 \right) . \tag{6}$$

In Eq. (6), α controls the curvature of the nonlinear function at non-positives. Figure 4 compared the curves of three non-positivity corrections, FL, TH and MPFs with different α values. In Fig. 4, as the parameter α goes up, the MPF function produces a larger bias from the offset-corrected sinogram over the entire range of the x-axis and the bias propagates into neighbors around non-positives through an error dispersion step. Thus, we need to set α carefully to preserve the true mean in the sinogram.

2. Analysis of Impact on Statistical Variance Model of CT Sinograms

The weight matrix $\boldsymbol{W}$ in a WLS reconstruction is inversely proportional to the statistical variance of the post-log projection data ($\boldsymbol{p}$). In reality, because approximating the post-log data variance from a single CT scan is inevitable, the post-log variance was approximated by using the pre-log data ($\boldsymbol{\lambda}$) and a first-order Taylor series expansion of the logarithm function [33]:

$$\boldsymbol{W} = \frac{1}{var[p]} = \frac{1}{var[\log\lambda]} \cong \frac{E^2[\lambda]}{var[\lambda]} . \tag{7}$$

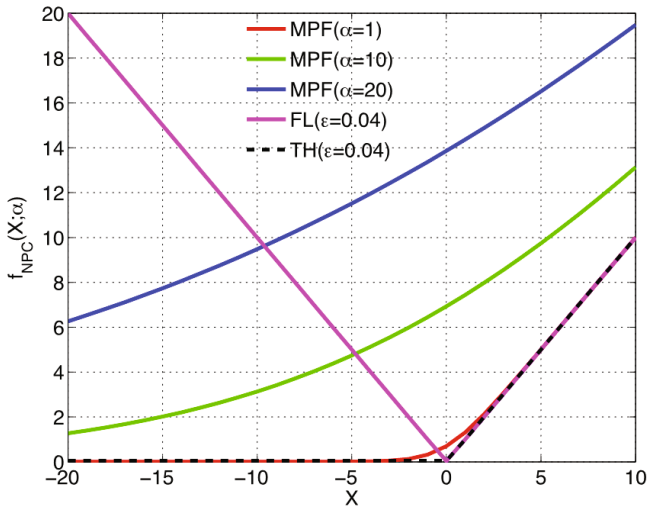

Fig. 4. Graphs of flip, truncation, and mean-preserving filters.

For the standard CT imaging protocol, assuming only a Poisson quantum noise model, which has the same mean ($m_{\rm Q}$) and variance on the pre-log data, the weight in Eq. (7) can be approximated to $m_{\rm Q}$:

$$\boldsymbol{W}_{\rm Q} = E[\boldsymbol{\lambda}] = m_{\rm Q} \approx \tilde{\boldsymbol{\lambda}} \; . \tag{8}$$

In practical WLS reconstruction, the weight matrix, $\boldsymbol{W}_{\rm Q}$, can be expressed approximately from the single measurement ($\tilde{\boldsymbol{\lambda}} = I_0 \exp(-\boldsymbol{p})$) of a random pre-log vector, $\boldsymbol{\lambda}$, in the intensity domain.

Because electronic noise is more dominant than quantum noise in extremely low-dose CT imaging, the Poisson quantum noise model in Eq. (8) does not match the real acquisition statistical properties [27]. Thibault *et al.* proposed a combined model of Poisson quantum and Gaussian electronic noises (Gaussian variance: σ_e^2) [33] and the weight matrix in Eq. (7) was approximated as follows:

$$\boldsymbol{W}_{\rm SQE} = \frac{E^2[\lambda]}{var[\lambda]} = \frac{m_{\rm Q}^2}{m_{\rm Q} + \sigma_e^2} \approx \frac{\tilde{\lambda}^2}{\tilde{\lambda} + \sigma_e^2} \; . \tag{9}$$

However, neither the quantum only ($\boldsymbol{W}_{\rm Q}$) model nor the combined quantum and electronic variance ($\boldsymbol{W}_{\rm SQE}$) model consider the impact of pre-corrections on statistical changes in the measured pre-log data. In Fig. 3, the non-positive correction changes the statistical properties such as the mean and the variance significantly especially in the extremely low-dose scenario. The difference between the true (red dotted line) and the sample (blue solid line) means was larger under an extremely low-dose, as shown in Figs. 3(e) and (f).

Here, we used the MPF non-positivity correction for the variance model analysis. Thibault's weight estimate in Eq. (9) was modified to include the effect of two successive processing steps, nonlinear non-positive conversion and error dispersion of MPF. Because $\tilde{\boldsymbol{\lambda}}$ is a function of a random vector $\tilde{\boldsymbol{X}}$, which is a sum of the offset-subtracted pre-log ($\boldsymbol{X}$) and the error dispersion ($\boldsymbol{E}$) random vectors, the variance of $\tilde{\boldsymbol{\lambda}}$ in the denominator of Eq. (9) can be approximated by using a Taylor expansion for the first and the second moments of the function as follows:

$$\begin{aligned} var[\tilde{\boldsymbol{\lambda}}] &= var[f_{\rm MPF}(\tilde{\boldsymbol{X}};\alpha)] \\ &\cong \{f'_{\rm MPF}(E[\tilde{\boldsymbol{X}}];\alpha)\}^2 var[\tilde{\boldsymbol{X}}] \; . \end{aligned} \tag{10}$$

The mean and the variance of $\tilde{\boldsymbol{X}} = \boldsymbol{X} + \boldsymbol{E}$ are

$$E[\tilde{\boldsymbol{X}}] = m_{\tilde{\boldsymbol{X}}} = E[\boldsymbol{X}] + E[\boldsymbol{E}] \approx f^{-1}_{\rm MPF}(\tilde{\lambda};\alpha) \; , \tag{11}$$

$$\begin{aligned} var[\tilde{\boldsymbol{X}}] &= \sigma^2_{\tilde{\boldsymbol{X}}} = var[\boldsymbol{X}] + var[\boldsymbol{E}] \\ &= m_{\rm Q} + \sigma_e^2 + \sigma_E^2 \; . \end{aligned} \tag{12}$$

The inverted and the first derivative forms of the MPF function are

$$f^{-1}_{\rm MPF}(X;\alpha) = \alpha \log\left(\exp\left(\frac{X}{\alpha}\right) - 1\right) \; , \tag{13}$$

$$f^{-1}_{\rm MPF}(X;\alpha) = \frac{\exp(X/\alpha)}{\exp(X/\alpha) + 1} \; . \tag{14}$$

For the i-th sinogram bin, the dispersed error $\boldsymbol{E}_i$ is computed as the weighted sum of changes in the preceding neighbors (N_i) that have been processed by using the MPF adjustment in Eq. (6) as follows

$$\begin{aligned} \boldsymbol{E}_i &= \sum_{n \in N_i} \omega_n \boldsymbol{\varepsilon}_n \\ &= \sum_{n \in N_i} \omega_n [\tilde{\boldsymbol{X}}_n - f_{\rm MPF}(\tilde{\boldsymbol{X}}_n;\alpha)] \\ &\triangleq \sum_{n \in N_i} \omega_n g_\alpha(\tilde{\boldsymbol{X}}_n) \; . \end{aligned} \tag{15}$$

If independent error random variables, $\boldsymbol{\varepsilon}_n$, of neighbors are assumed, the variance of $\boldsymbol{E}_i$ can be approximated as follows:

$$\sigma^2_{E_i} \triangleq var[\boldsymbol{E}_i] \cong \sum_{n \in N_i} \omega_n^2 var[\boldsymbol{\varepsilon}_n] \; . \tag{16}$$

The variance of each neighbor, $\boldsymbol{\varepsilon}_n$, is

$$\begin{aligned} \sigma^2_{\boldsymbol{\varepsilon}_n} &\triangleq var[\boldsymbol{\varepsilon}_n] \cong [g'_\alpha | \tilde{\boldsymbol{X}}_n = m_{\tilde{\boldsymbol{X}}_n}]^2 \sigma^2_{\tilde{\boldsymbol{X}}_n} \\ &= \left[1 - f'_{\rm MPF}(m_{\tilde{\boldsymbol{X}}_n};\alpha)\right]^2 \sigma^2_{\tilde{\boldsymbol{X}}_n} \; . \end{aligned} \tag{17}$$

With Eqs. (12) and (17), the variance of $\tilde{\boldsymbol{X}}_i$ can be practically computed as

$$var[\tilde{\boldsymbol{X}}_i] \cong \tilde{\boldsymbol{X}}_i - \boldsymbol{E}_i + \sigma_e^2 + \sum_{n \in N_i} \omega_n^2 \sigma^2_{\boldsymbol{\varepsilon}_n} \; , \tag{18}$$

with the approximation $m_{\rm Q} \cong \boldsymbol{X} = \tilde{\boldsymbol{X}} - \boldsymbol{E}$. The advanced weight matrix considering quantum and electronic noises and the effect of MPF can be approximated as follows:

$$\boldsymbol{W}_{\rm AQE} = \frac{E^2[\tilde{\lambda}]}{var[\tilde{\lambda}]} \cong \frac{\tilde{\lambda}^2}{\{f'_{\rm MPF}(\tilde{\boldsymbol{X}};\alpha)\}^2 \{\tilde{\boldsymbol{X}} - \boldsymbol{E} + \sigma_e^2 + \sigma_{\boldsymbol{E}}^2\}} \; . \tag{19}$$

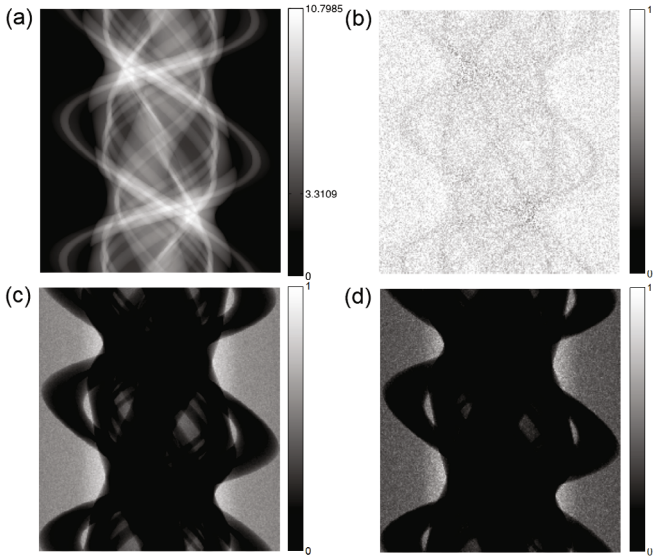

Fig. 5. Mean-to-variance ratio of 1000 simulated sonograms: (a) noisefree sinogram, (b) Poisson-only quantum noise, (c) Gaussian electronic noise ($\sigma_e = 15$), and (d) Gaussian electronic noise ($\sigma_e = 22$).

3. CatSim Simulation and Evaluation

CT simulations were performed using the NCAT chest phantom and the CatSim simulator [34], which generates poly-energetic compound Poisson data (0.5 mAs and 80 kVp) with Gaussian electronic noise ($m_e = 897$, $\sigma_e^2 = 0, 15^2, 22^2$). We simulated 1000 independent sinograms under each noise level and then applied offset subtractions and three different non-positivity correction methods for the log-conversion. Figure 5 shows the noise-free sinogram (a) and three different noise levels in terms of the mean-to-variance ratio (b to d) in the pre-log domain after offset subtraction. To compute the mean-to-variance ratio, we used noise-free and sample variance sinograms over 1000 realizations as the mean and the variance, respectively. In comparison to Fig. 5(a) in the case of Poisson-only quantum noise having most ratio values around one, Figs. 5(b) and (c) show increased variances due to Gaussian noise. For the non-positivity correction, the flip and the truncation methods replaced the non-positives or zeros with 0.04 of the threshold before log-conversion. In MPF, the parameter α was set to 1 and 20 for Poisson-only and addition of Gaussian noises, respectively.

For the quantitative comparison of different non-positivity correction methods in the sinogram, we evaluated the mean signed deviation (MSD) over multiple realizations as follows:

$$MSD = \frac{1}{R}\sum_{r=1}^{R}\frac{1}{N}\sum_{i=1}^{N}\frac{1}{N}\boldsymbol{P}_{i;r}^{\mathrm{NPC}} - \boldsymbol{P}_{i,r}^{\mathrm{Noise-free}} \ . \quad (20)$$

In Eq. (20), R and N are the numbers of realizations and the post-log sinogram elements, and the ground truth of the sinogram ($\boldsymbol{P}^{\mathrm{Noise-free}}$) was a noise-free post-log sinogram. Also, for the quantitative comparison of the reconstructed images from different pre-corrections and noise levels, MSDs in Eq. (20) were evaluated over 1000 realizations and over a specific region-of-interest, *e.g.*, bone on the left arm. For the MSD computation of the reconstructed images, we replaced $\boldsymbol{P}^{\mathrm{Noise-free}}$ with $\boldsymbol{\mu}_{\mathrm{Truth}}$, which was obtained from the unweighted least squares reconstruction with 50 iterations of a noise-free sinogram.

Through simulation of 1000 independent sinograms under each noise level, we computed the sample variances of the post-log data, and we applied the sample variances to the WLS reconstruction as the best possible weight matrices.

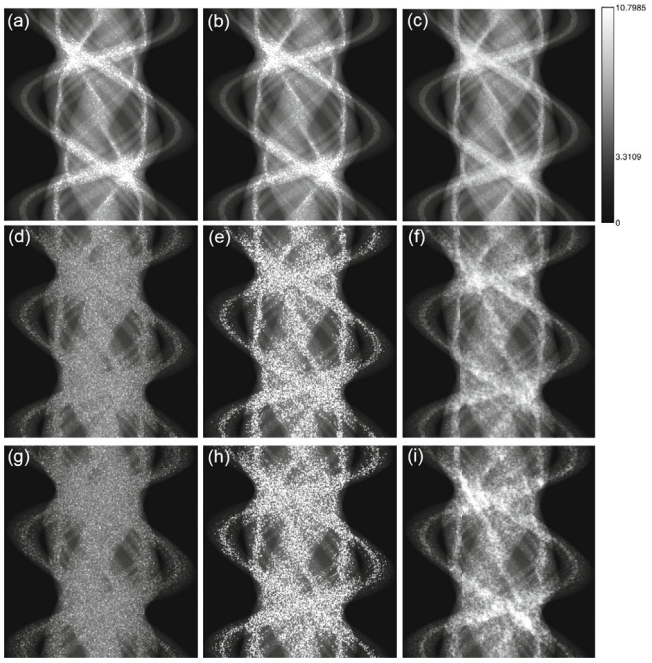

Fig. 6. Post-log sinograms after three different non-positive correction methods, flip (left), truncation (middle), and mean-preserving filter (right column) under three different noise levels: (a to c) Poisson-only quantum noise, (d to f) Gaussian electronic noise ($\sigma_e = 15$), and (g to i) Gaussian electronic noise ($\sigma_e = 22$).

III. RESULTS

We analyzed the statistical properties, mean and variance, by using three different non-positive correction methods and the variance estimating methods in weighted least-squares reconstruction. Figure 6 shows post-log sinograms after having applied three different non-positive corrections and log-conversion under different noise levels. Three rows from the top to the bottom contain different Gaussian noise levels, $\sigma_e = 0$, 15, 22,

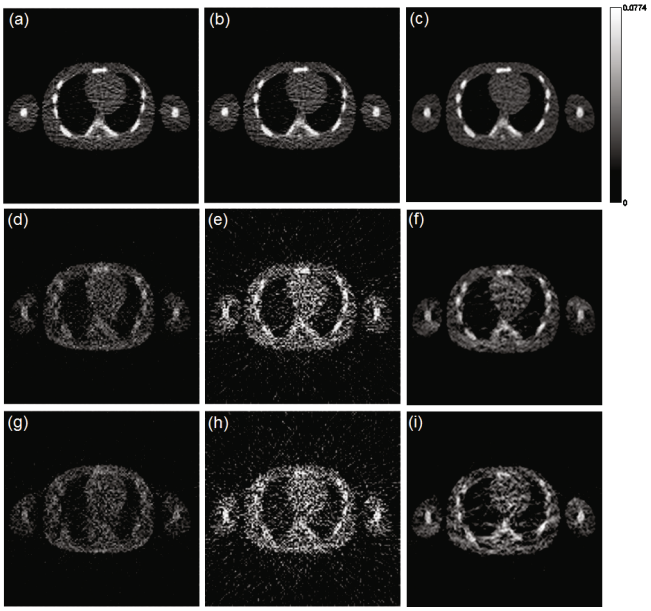

Fig. 7. FBP reconstructions with a ramp filter of post-log sinograms after three different non-positive correction methods, flip (left), truncation (middle), and mean-preserving filter (right column) under three different noise levels: (a to c) Poisson-only quantum noise, (d to f) Gaussian electronic noise (σ_e = 15), and (g to i) Gaussian electronic noise (σ_e = 22).

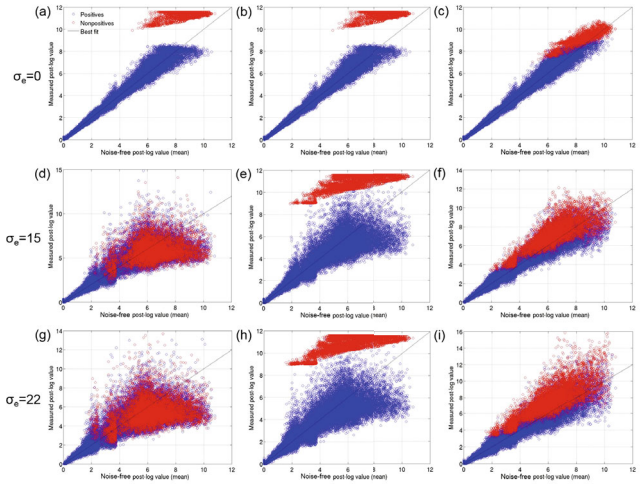

Fig. 8. Scatter plots of noisefree versus non-positive corrected post-log sinograms through three different methods, flip (left), truncation (middle), and mean-preserving filter (right column) under three different noise levels; (a to c) Poisson-only quantum noise, (d to f) Gaussian electronic noise (σ_e = 15), and (g to i) Gaussian electronic noise (σ_e = 22). (red: non-positive values, blue: postives).

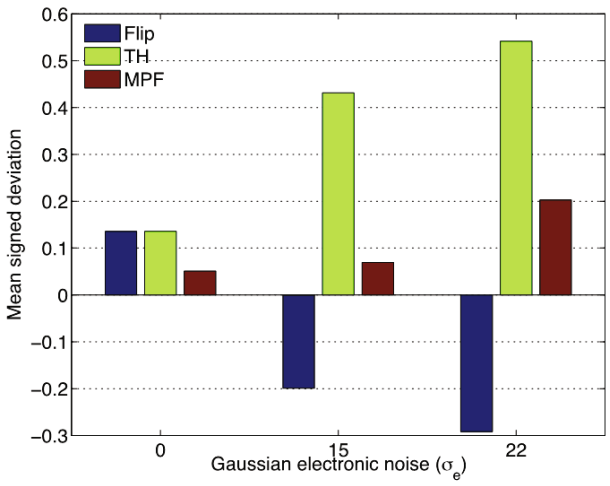

Fig. 9. Mean signed deviation graph of three non-positive correct methods, flip (blue), truncation (green), and mean-preserving filter (red) under three different noise levels: Poisson-only quantum noise (σ_e = 0) and two Gaussian electronic noise levels (σ_e = 15 and 22).

respectively. Left to right columns correspond to flip, truncation (TH), and mean preserving filter (MPF), respectively. Visually, as shown in the far right column in Fig. 6, MPF resulted in slight blurring and the better signal-to-noise ratio than the flip and the truncation methods as data became noisier. The flip and the truncation methods took on different aspects on the sinogram elements undergoing high attenuation through dense material like bone because the negative values increased with higher Gaussian noise (Figs. 6(d) vs (e) or Figs. 6(g) vs (h)). Flip leads to an under-bias because the negative values are inverted to positives through an absolute operation, and the corrected absolute values contribute to the post-log values being lower than the truth (noise-free sinogram) through log-conversion (lost contrast of bone-attenuating elements on (d) and (g) in far left column of Fig. 6). Meanwhile, the truncation method is over-biased because the corrected negatives are concentrated at a threshold that will be the highest post-log value (the bright spots on (e) and (h) in the middle column of Fig. 6). Figure 7 compares the filtered back-projection (FBP) images of the corresponding post-log signograms in Fig. 6. The under- or over-biased effects were propagated to the reconstructed images showing low contrast or overshooting image intensities after the flip or the truncation correction methods.

These different bias patterns over non-positive correction methods are shown well in Fig. 8, which shows scatter plots of the corrected post-log sinogram entries in Fig. 6 over the truth (noise-free). Blue and red dots indicate positives and non-positives, respectively. Top to bottom rows are different Gaussian noise levels, σ_e = 0, 15, 22. Left to right columns are different non-positive correction methods, flip, truncation, and MPF. In the scatter plot for the flip method, the non-positives simply overlapped the positives and caused under-biases at high post-log entries. In the truncation plots, the over-bias appeared in the gathered threshold values (red). The threshold values in the post-log domain vary due

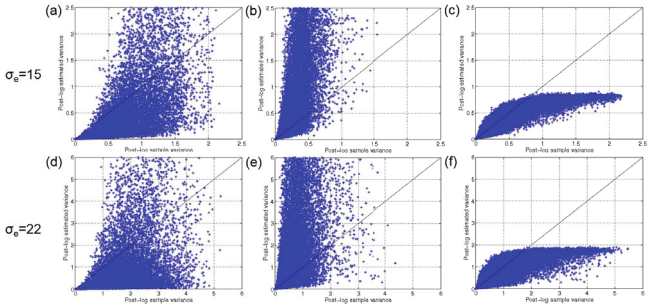

Fig. 10. Scatter plots of best possible post-log variance (sample variance over 1000 realizations) versus three variance estimates from Poisson-only (W_{Q}, left), simple Gaussian electronic (W_{SQE}, middle), and advanced Gaussian electronic (W_{AQE}, right column) based variance models under two Gaussian electronic noise levels (σ_e = 15 (a to c) and 22 (d to f)).

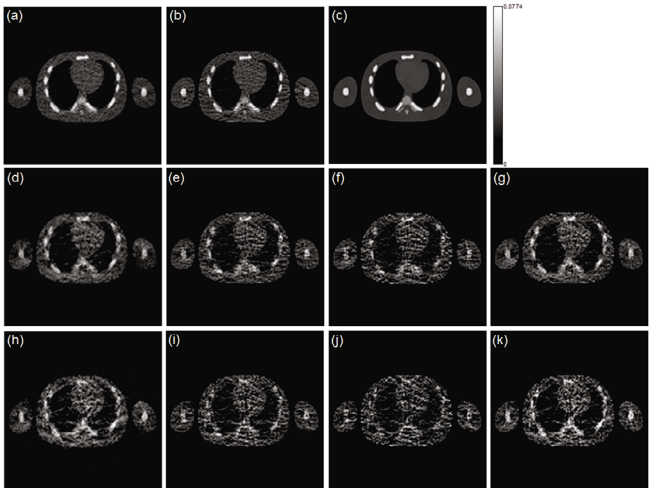

Fig. 11. Comparison reconstructions from FBP with Ramp (1st column), WLSs with W_{Q} (2nd), W_{SQE} (3rd), and W_{AQE} (4th column) with truth image (c) from unweighted least-squares reconstruction under Poisson-only noise and Gaussian electronic noise levels (σ_e = 0 (a to b), 15 (d to g), and 22 (h to k)).

to the X-ray influx being filtered by bowtie through log-conversion. MPF provided the expected overall distribution shape with proper statistical properties by gathering all post-log entries around identity (black line) and making the scatter wider around higher identity (high post-log values) due to the proper contribution of the corrected non-positives.

Figure 9 compared the mean signed deviations of flip (blue), truncation (green), MPF (red) under different noise levels. Larger mean signed deviation indicates more bias from the noise-free sinogram after non-positive correction. For all electronic noise levels, MPF produced the smallest mean signed deviations compared to Flip and TH. MPF shows an up to five times reduction in the mean signed deviation compared to the truncation method when Gaussian electronic noise level is 15. Flip and truncation tend to be under- and over-biased, respectively, when the electronic noise is added.

Figure 10 showed scatter plots of the post-log variance estimated from three noise models, $\boldsymbol{W}_{\mathrm{Q}}$, $\boldsymbol{W}_{\mathrm{SQE}}$, and $\boldsymbol{W}_{\mathrm{AQE}}$, in the left to right columns, respectively. The x-axis of the scatter plots is ground-truth variance ($\boldsymbol{W}_{\mathrm{Best}}$), which is the sample variance over 1000 corrected post-log simulation data. The y-axis is the variance computed from a single pre-corrected measurement (MPF with α = 20) under different electronic noise levels (σ_e = 15 and 22) from top to bottom in Fig. 10. The simple combined Poisson and Gaussian noise model, $\boldsymbol{W}_{\mathrm{SQE}}$ (b and f), showed the most highly biased variance even compared to the Poisson-only model, $\boldsymbol{W}_{\mathrm{Q}}$ (a and d). However, the variance from our proposed model, $\boldsymbol{W}_{\mathrm{AQE}}$ (c and f), which includes the effect of MPF on the post-log variance, as well as electronic noise, best matched the variance than either $\boldsymbol{W}_{\mathrm{Q}}$ or $\boldsymbol{W}_{\mathrm{SQE}}$, although it still was biased at high variance. The biased variance results from an approximation of pre-log variance in the denominator of Eq. (19).

Figure 11 compares the image quality of FBP with a ramp filter to WLS reconstructions. WLS reconstructions with three different weight matrices were performed by using 10 iterations to reconstruct the simulated data at a low-dose protocal of 0.5 mAs. MPF (α = 1 or 20) was applied to the offset-corrected pre-log data. In Fig. 11, FBP-Ramp (a) and WLS-W_{Q} (b) reconstructions showed similar visual image quality in the case of no electronic noise (Poisson-only) in the simulation data. However, as the electronic noise becomes more dominant in the sonogram (the middle and bottom rows in Fig. 11), WLSs with inappropriate variances ($\boldsymbol{W}_{\mathrm{Q}}$ (e and i) and $\boldsymbol{W}_{\mathrm{SQE}}$ (f and j)) resulted in worse image quality than FBPs (d and h). With the advanced variance, $\boldsymbol{W}_{\mathrm{AQE}}$, WLS can provide a robust image to the electronic noise as shown in Figs. (g) and (k). We could see the improvement from $\boldsymbol{W}_{\mathrm{AQE}}$ in terms of the MSD in Fig. 12. Figure 12(a) is the MSDs over the entire image region and (b) is over the bone of the left arm. Except for our proposed model $\boldsymbol{W}_{\mathrm{AQE}}$, the greater the electronic noise, the more the MSD from FBP, $\boldsymbol{W}_{\mathrm{Q}}$ and $\boldsymbol{W}_{\mathrm{SQE}}$ increased. In Fig. 12(b), the dense signal such as bone was recovered well with $\boldsymbol{W}_{\mathrm{AQE}}$ as the electronic noise was increased.

Figure 13 compares the FBP to the penalized WLS (PWLS) reconstructions under two different tube currents (0.5 and 10 mAs) and a fixed electronic noise level (σ_e = 15). WLS-WQ reconstructed a control image (a) from normal dose data under assumptions of no electronic noise and tube current of 400 mAs. The truncation method was applied prior to all FBP reconstructions (b) and (c). All PWLS reconstructions, (d) to (i), were obtained with smooth penalty after the MPF correction. In the second and the third rows of the PWLS results, the left to right columns correspond to the PWLS results with different variance models, Q-only and simple and advanced QE, respectively. At the lower dose, 0.5

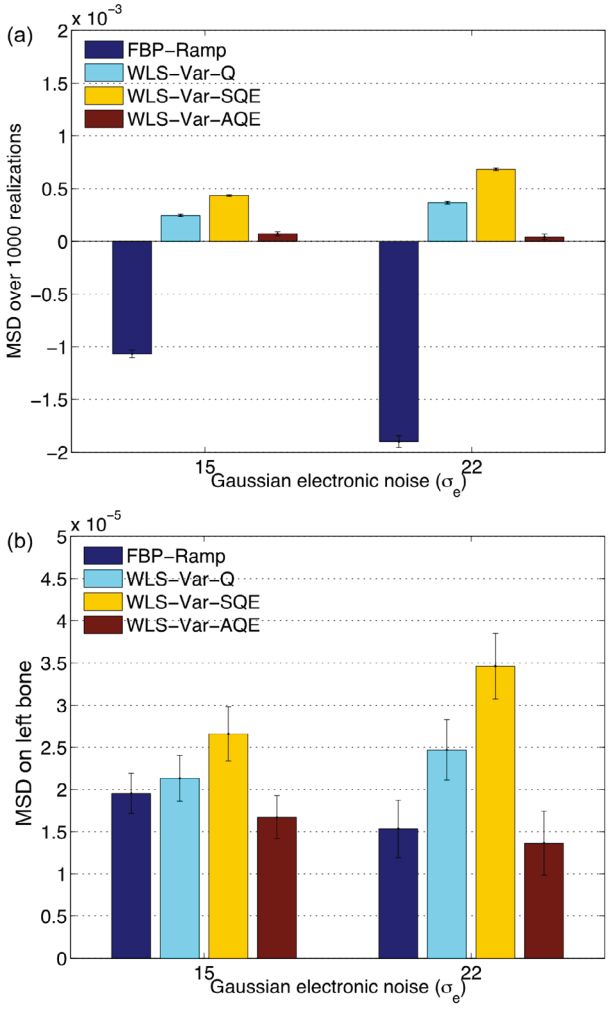

Fig. 12. Mean signed deviation graphs of FBP-Ramp and WLS reconstructions over (a) entire image domain and (b) bone region.

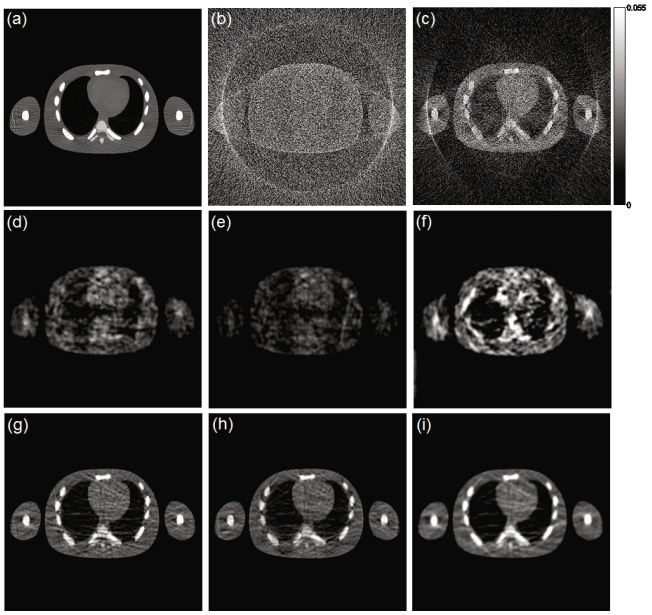

Fig. 13. Comparison of reconstructions from FBPs and PWLS reconstructions with different weight estimates under two different tube currents and Gaussian electronic noise level, $\sigma_e = 15$: (a) control (400 mAs, WLS-Q), (b) FBP (Threshold, 0.5 mAs), (c) FBP (Threshold, 10 mAs), (d) PWLS-Q (0.5 mAs, $\beta = 10^8$), (e) PWLS-SQE (0.5 mAs, $\beta = 10^6$), (f) PWLS-AQE (0.5 mAs, $\beta = 5 \times 10^7$) , (g) PWLS-Q (10 mAs, $\beta = 10^6$), (h) PWLS-SQE (10 mAs, $\beta = 10^5$), and (i) PWLS-AQE (10 mAs, $\beta = 5 \times 10^6$). β is the strength of the penalty function for PWLS.

mAs, PWLS-AQE resulted in a better recovered dense signal, such as from bone, compared to the other two variance models.

IV. DISCUSSION

We analyzed the impacts of non-positive corrections and the noise models on the mean and the variance of the post-log data in extremely low-dose CT imaging. CatSim simulated low-dose CT measurements with different noise models: of Poisson-only and adding Gaussian electronic noise with standard deviations of 15 and 22. Two successive processing steps of nonlinear conversion and error dispersion in the MPF helped to maintain the original mean of the raw measurement better than the other flip and truncation methods. The nonlinearity of the MPF causes the nonpositives to change smoothly.

Figure 12 shows noisy and biased variances computed from a single measurement under an extremely low-dose protocol. In the comparison of the variance estimates, the simple weight matrix considering electronic noise only ($\boldsymbol{W}_{\mathrm{SQE}}$) in Eq. (9) was the worst due to its ignoring the significant variance changes from the MPF. The modified variance estimate ($\boldsymbol{W}_{\mathrm{AQE}}$), including the impact MPF on the original variance in Eq. (19), recovered the signal of the dense materials such as bone better. However, $\boldsymbol{W}_{\mathrm{AQE}}$ still was under-biased at high variance (as demonstrated in Figs. 10(c) and (f)) due to an approximation of the denominator in Eq. (19). Although our proposed variance model limits the estimate accuracy at high variance, it almost recovers a visually image quality close to the best weight matrix derived from multiple realizations (which is not possible in reality) at extremely low-dose.

In Fig. 13, compared to the conventional CT image reconstructions of FBP after truncation method and WLS with Poisson-only noise model ($\boldsymbol{W}_{\mathrm{Q}}$) after MPF, the combination of MPF and WLS with the better variance estimate from a single measurement acquisition is seem to improve the maximum image quality, which is an inherent limitation of the WLS reconstruction derived from a Gaussian post-log distribution.

V. CONCLUSION

For the simulated extremely low-dose scenario of 80 kVp and 0.5 mAs with a chest phantom, MPF improved the bias of post-log data by up to roughly five times compared to the conventional threshold and flip methods. Simple weights, even those including an electronic noise model, in a WLS reconstruction that neglected the effect of non-positive correction produced limited improvement in the image quality. The advanced weight matrix from a single measurement considering electronic noise and the effect of a non-positivity correction on the variance change recovered the image signal of dense materials such as bone better. However, the improvement in image quality from a WLS reconstruction based on a Gaussian post-log distribution for extremely low-dose CT imaging is inherently limited. Different statistical models for the pre-log distribution or recent deep learning reconstruction methods could be adopted to overcome the inherent limitation.

ACKNOWLEDGMENTS

The authors gratefully acknowledge the helpful discussions of Adam Alessio, Jean-Baptiste Thibault and Ruoqiao Zhang and the CatSim from Bruno De man. This work is supported by the National Institutes of Health [grant numbers R01-CA115870, R01-HL109327], and by the National Research Foundation of Korea [grant number NRF-2018R1D1A1B07049296].

REFERENCES

[1] N. Buls, J. Pagés, J. de Mey and M. Osteaux, Health Phys. **85**, 165 (2003).
[2] J. R. Mayo, J. Aldrich, N. L. Muller and S. Fleischner, Radiology **228**, 15 (2003).
[3] E. J. Hall and D. J. Brenner, Br. J. Radiol. **81**, 362 (2008).
[4] W. W. Mayo-Smith *et al.*, Radiology **273**, 657 (2014).
[5] L. Zhou, S. Bai, Y. Zhang and J. Deng, Med. Phys. **42**, 3265 (2015).
[6] M. M. Rehani, Radiat. Prot. Dosim. **165**, 3 (2015).
[7] H. Imhof *et al.*, Eur. J. Radiol. **47**, 29 (2003).
[8] J. F. Paul and H. T. Abada, Eur. Radiol. **17**, 2028 (2007).
[9] M. Mahesh, Pediatr. Radiol. **41**, 493 (2011).
[10] A. K. Hara *et al.*, AJR Am. J. Roentgenol. **201**, 33 (2013).
[11] S. Trattner *et al.*, J. Am. Coll. Radiol. **11**, 271 (2014).
[12] J. Lambert, J. D. MacKenzie, D. D. Cody and R. Gould, J. Am. Coll. Radiol. **11**, 262 (2014).
[13] T. Xia *et al.*, Phys. Med. Biol. **57**, 309 (2012).
[14] J. Hsieh, Med. Phys. **2**, 139 (1998).
[15] J. Wang, T. Li, H. Lu and Z. Liang, IEEE Trans. Med. Imaging **25**, 1272 (2006).
[16] J. Wang, H. Lu, J. Wen and Z. Liang, IEEE Trans. Biomed. Eng. **55**, 1022 (2008).
[17] A. Manduca *et al.*, Med. Phys. **36**, 4911 (2009).
[18] H. Zhang *et al.*, Med. Phys. **41**, 031906 (2014).
[19] M. Bai *et al.*, Med. Phys. **36**, 95 (2009).
[20] Z. Li *et al.*, Med. Phys. **41**, 011908 (2014).
[21] I. A. Elbakri and J. A. Fessler, IEEE Trans. Med. Imaging **21**, 89 (2002).
[22] J. B. Thibault, K. D. Sauer, C. A. Bouman and J. Hsieh, Med. Phys. **45**, 4526 (2007).
[23] B. Kataria and O. Smedby, Acta Radiol. **54**, 540 (2013).
[24] N. Buls, *et al.*, Eur. Radiol. **25**, 1023 (2014).
[25] T. Klink *et al.*, Eur. J. Radiol. **83**, 1654 (2014).
[26] E. Hérin *et al.*, Eur. Radiol. **25**, 2362 (2015).
[27] J. Nuyts *et al.*, Phys. Med. Biol. **58**, R63 (2013).
[28] L. Fu *et al.*, IEEE Trans. Med. Imaging **36**, 707 (2017).
[29] B. R. Whiting, Proc. SPIE Med. Imaging **4682**, 53 (2002).
[30] B. R. Whiting *et al.*, Med. Phys. **33**, 3290 (2006).
[31] S. Zabić, Q. Wang, T. Morton and K. M. Brown, Med. Phys. **40**, 031102 (2013).
[32] K. Sauer and C. Bouman, IEEE Trans. Signal Process. **41**, 534 (1993).
[33] J. B. Thibault, C. A. Bouman, K. D. Sauer and J. Hsieh, Proc. SPIE Comput. Imaging IV **6065**, 60650X (2006).
[34] B. De Man *et al.*, Proc. SPIE Med. Imaging: Phys. Med. Imaging **6510**, 65102G (2007).